Check for updates

Two-dimensional hexagonal boron nitride nanosheet as the planar-alignment agent in a liquid crystal-based electro-optic device

RAJRATAN BASU* AND LUKAS J. ATWOOD

Department of Physics, Soft Matter and Nanomaterials Laboratory, The United States Naval Academy, Annapolis, MD 21402, USA
basu@usna.edu

Abstract: The planar-alignment agent in an electro-optic liquid crystal (LC) device plays an essential role for the LC's electro-optical characteristics. Rubbed polyimide (PI) layers are conventionally used as the planar-alignment agent in traditional liquid crystal displays (LCDs). Here we experimentally demonstrate that the 2D hexagonal boron nitride (h-BN) nanosheet can serve as the planar-alignment agent in an LC cell. This h-BN has higher chemical stability and more optical transparency than the PI layer. Two h-BN-covered indium tin oxide (ITO) glass slides (without any conventional PI layers) are placed together to fabricate an LC cell. A nematic LC inside this h-BN-based cell exhibits uniform planar-alignment—which is probed by a crossed polarized optical microscope. This planar-alignment at the molecular scale is achieved due to the coherent overlay of the benzene rings of the LC molecules on the hexagonal BN lattice. This h-BN-based LC cell shows the typical electro-optical effect when an electric field is applied via ITO electrodes. The dielectric measurement across this h-BN-based electro-optic cell shows a standard Fréedericksz transition of the LC, confirming that the 2D h-BN, as the planar-alignment agent, supplies adequate anchoring energy—which can be overcome by the Fréedericksz threshold voltage. Finally, we show that the h-BN-based LC cell exhibits more optical transparency than a regular PI alignment layer-based LC cell.

1. Introduction

Liquid crystals (LCs) are optically anisotropic materials, and they are widely used in electro-optical display technology. Understanding the alignment phenomena of a nematic LC on a surface remains an important area of research, as the alignment process determines the LC's molecular orientation and conformation—which influence the LC's optical and electro-optical characteristics [1]. For example, semi-transparent LC cells are used in optically transmissive liquid crystal displays (LCDs), where the planar-alignment layers are utilized to create an easy axis of the nematic director ($\hat{n}$) of the LC. These planar-alignment layers are also required in other LC devices, such as LC-based optical and chemical sensors [2]. Therefore, studying the alignment phenomena of the LC on a substrate is fundamentally important for potential applications of optically transmissive LC devices.

The conventional planar-alignment layer is a rubbed polyimide (PI)-coated surface [3]. On the unidirectionally rubbed PI alignment substrate, the LC molecules align with alkyl side chains along the rubbing direction, creating a uniform planar director profile on the substrate [3]. However, the conventional rubbed PI alignment process has some disadvantages. The temperature during the rubbing process of the PI has a significant impact on the LC alignment [4]. The occurrence of fiber dust during the rubbing process of the PI [1] contaminates the LC. Uneven rubbing creates a wide distribution of pre-tilt angles of the LC—which causes a non-uniform brightness in the LCD panel [1]. The PI alignment layers can inject free ion impurities into the LC [5]. Other problems of the rubbing process on the PI substrate include difficulties of status monitoring [1] and lack of controllability [1]. Therefore, studying various LC-substrate interactions, and then, developing alternate LC alignment methods (*e.g.*, oblique

SiO evaporation [1], microgroove grating surface fabrication [1], photoalignment technology [6], etc.) is an important research direction for optical display applications.

Here we report an interesting phenomenon of two-dimensional (2D) *hexagonal boron nitride* (*h*-BN)-induced planar-alignment of a nematic LC and the subsequent optical and electro-optical effects. The sp^2 conjugated 2D boron nitride nanosheet forms a honeycomb structure of alternating boron and nitrogen atoms with a lattice spacing of 1.44 Å [7]. This 2D *h*-BN is an insulator [8], which has a very high structural [9], thermal [10], and chemical [11] stability. Due to these excellent properties, this ultra-flat 2D *h*-BN is often used as a dielectric substrate in nano-electronic devices [12–14]. In our experiment, the LC achieves a uniform planar-aligned state in-between two *h*-BN nanosheets due to the interesting epitaxial interaction between the hexagonal lattice of *h*-BN and the benzene rings of the LC molecules. This *h*-BN-induced planar-alignment was probed by a crossed polarized microscope. We then demonstrate the electro-optical operations of an LC cell where the *h*-BN is employed as the planar-alignment agent. This investigation also falls in the current theme of research of the application of 2D materials in various optoelectronic devices [15–17].

2. Experiments, results, and discussion

In this section, we present (a) the fabrication of the *h*-BN based planar LC cell, (b) the electro-optical effect of the LC in the cell, (c) measurements of the LC parameters in this electro-optic cell, and finally, (d) the optical transmission spectroscopy of the cell.

2.1 Fabrication of the electro-optic LC cell employing 2D h-BN as the planar-alignment agent

In an *h*-BN lattice, the B—N bond length is 1.44 Å [7]. In a hexagonal benzene ring, the C—C bond length is 1.40 Å. Therefore, the hexagon of the benzene ring and the hexagon in the *h*-BN lattice have almost the same size. It has been experimentally demonstrated that due to this nano-architectural symmetry of the hexagons in both the species, the benzene rings of the LC coherently align on the hexagonal lattice of *h*-BN [18]. The interactions between the nematic LC and the hexagonal lattice of other different nanomaterials (*e.g.*, graphene, carbon nanotube, molybdenum diselenide, tungsten diselenide) [19–29] have also demonstrated that the LC can achieve a planar-aligned state on the hexagonal nanosurface. The density functional calculations showed that this planar anchoring of the LC on the hexagonal nanostructure is further strengthened with a binding energy, ranging from 0.7 to 2.0 eV/molecule [21,27,39], by the electrostatic energy resulting from a considerable amount of charge transfer between the LC molecules and the hexagonal lattice structure. This spontaneous alignment mechanism of the LC on the hexagonal lattice is the fundamental principle in our experiment for using the 2D *h*-BN as the planar-alignment agent in this electro-optic LC device. A single *h*-BN 2D crystal, the LC molecules can obtain three different orientations separated by 60 degrees due to the hexagonal symmetry.

This three-fold alignment degeneracy is illustrated in Figs. 1(a), 1(b), and 1(c). The epitaxial interaction between the LC and the *h*-BN lattice is illustrated by the overlay of the LC's benzene rings on the *h*-BN-honeycomb structure. We have carried out the following experiments to understand the size of the degenerate domains. Chemical Vapor Deposition (CVD) grown monolayer *h*-BN film on a copper foil was obtained from Graphene Supermarket, Inc. The presence of monolayer *h*-BN on the copper foil was verified by the Raman spectroscopy, as shown in Fig. 1(d). The standard polymethyl-methacrylate (PMMA) assisted wet transfer method [30,31] was used to transfer the monolayer *h*-BN film from the copper foil onto several 2.5×2.5 cm^2 ITO coated glass substrates. The Tunneling Electron Microscope (TEM) analysis from the manufacturer provided the hexagonal crystal direction of the monolayer *h*-BN film on the copper foil. This orientation was roughly maintained during the wet transfer method. To realize the alignment degeneracy, a thin LC layer was created by placing a small droplet of liquid crystal E7 (T_{NI} = 60.5 °C, *EMD Millipore*

Corporation) on the transferred *h*-BN film on the ITO slide and then gently blowing the droplet away by a dust blower. The thin LC layer on the *h*-BN sample was heated up (to the isotropic phase) and cooled down (to the nematic phase) multiple times to remove any remaining order resulted from the coating process. A crossed polarized optical microscope (Olympus BX61) was used to study the alignment of the LC at several locations on the *h*-BN film on the ITO slide. It is known that a *bright* uniform texture with a maximum transmitted intensity through an LC layer appears when the uniform planar-aligned $\hat{n}$ is at 45° with the crossed polarizers. A *dark* uniform texture is achieved if $\hat{n}$ is parallel to the polarizer (or to the crossed analyzer). Since an abrupt directional change of $\hat{n}$ occurs at the degenerate domain boundaries, the degenerate domains can be clearly seen in the micrographs in Figs. 1(e), 1(f), 1(g), and 1(h). When the sample was rotated through 45° under the crossed polarized microscope, the degenerate domains changed their intensities, as shown in the micrographs. The size of each micrograph is ~1.2 × 0.85 mm². Therefore, it clearly demonstrates that even with the alignment degeneracy, it is possible to get a reasonably large (more than half the size of the micrograph) uniform LC domain with unidirectional planar-alignment on the *h*-BN film. From the application point of view, in the modern high-resolution LCDs, the typical pixel width is ~250 *μ*m or less [32]. Therefore, it could be possible to employ the *h*-BN nanosheet as the planar-alignment agent in individual pixels as long as a uniform domain size is more than a pixel's dimension in the LCD.
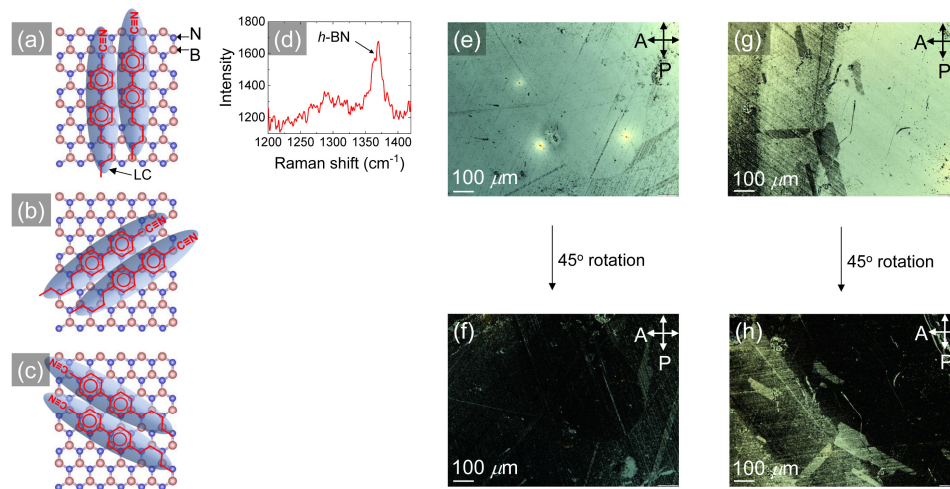

Fig. 1. (a), (b), (c) The alignment of nematic LC molecules (ellipsoids) on 2D *h*-BN (honeycomb structure) is illustrated. The epitaxial interaction between the LC and the *h*-BN lattice is schematically shown by matching the LC's benzene rings on the *h*-BN-honeycomb structure. The *three-fold alignment degeneracy* is illustrated as the nematic director, $\hat{n}$ is orientated at (a) 0°, (b) + 60°, (c) −60°, with the vertical. (d) Raman signal of monolayer *h*-BN on copper foil. (e) Microphotograph of a thin layer of nematic LC E7 on the *h*-BN film on the ITO slide under the crossed polarized microscope. (f) Micrograph of the LC sample when rotated by 45° under the crossed polarized microscope. (g), (h) Micrograph of the same LC sample at a different location and its 45° rotated state, respectively.

First, two ITO-only coated glass slides (without any PI layers or *h*-BN film) were placed together to make a cell with an average cell-gap, $d = 9$ *μ*m. This ITO-only cell was filled with LC E7. The micrographs in Figs. 2(a) and 2(b) present the LC texture in the ITO-only LC cell under the crossed polarized optical microscope. The micrographs clearly show that the LC

does not achieve a uniform planar-aligned state in the ITO-only cell, as multiple bright and dark textures appear in the micrographs.

The *h*-BN-based cells were prepared by placing together two *h*-BN/ITO glass substrates with the *h*-BN sides facing each other. We had to make several trial cells to achieve good uniform planar-alignment. When the two *h*-BN nanosheets do not align with each other in the same manner, the degenerate LC domains appear throughout the cell, and a uniform planar-aligned state is not achieved. The LC textures in three such *h*-BN/ITO cells are shown in Fig. 2. Figures 2(c) and 2(d) show the LC texture in the *h*-BN/ITO cell-1, where the LC shows degenerate planar-alignment. The *h*-BN/ITO cell-2 also shows degenerate planar-alignment in Figs. 2(e) and 2(f). Now note that in Figs. 2(g) and 2(h), the alignment-degeneracy is reduced significantly in the *h*-BN/ITO cell-3 as the orientation of the two *h*-BN nanosheets in the cell are not too far off from each other.

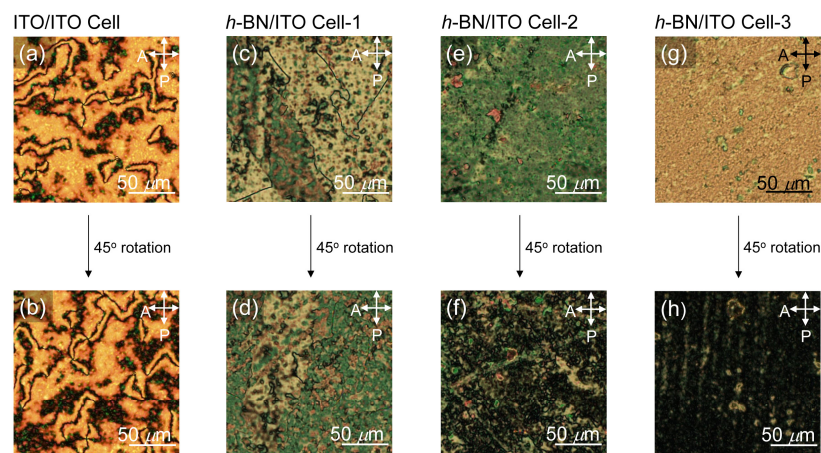ITO/ITO Cell   *h*-BN/ITO Cell-1   *h*-BN/ITO Cell-2   *h*-BN/ITO Cell-3

Fig. 2. (a), (b) The micrograph of LC E7 in the ITO-only cell under the crossed polarized microscope, and its 45° rotated state, respectively. (c), (d) The micrograph of LC E7 in the *h*-BN/ITO cell-1 under the crossed polarized microscope, and its 45° rotated state, respectively. (e), (f) The micrograph of LC E7 in the *h*-BN/ITO cell-2 under the crossed polarized microscope, and its 45° rotated state, respectively. (g), (h) The micrograph of LC E7 in the *h*-BN/ITO cell-2 under the crossed polarized microscope, and its 45° rotated state, respectively.

After several trials, we were finally able to make an *h*-BN/ITO LC cell (with $d = 9$ μm) where the two *h*-BN nanosheets were aligned reasonably well with each other. Figure 3(a) shows the LC texture of a large area in this cell. Overall, it shows a bright uniform texture of the LC as $\hat{n}$ is at 45° with respect to the crossed polarizers. Since this *h*-BN/ITO LC cell showed the best uniform planar-alignment, we performed the rest of the experiments using this cell. Note that there are still occasional dark patches in Fig. 3(a) from the alignment degeneracy. Therefore, we have used the dotted square area (*i.e.*, the region without any dark patches) in Fig. 3(a) for further analysis. Figure 3(b) shows a schematic representation of the *h*-BN/ITO cell where the two *h*-BN nanosheets are well-aligned with each other and the LC domain in-between maintains a uniform planar-alignment. To investigate the LC alignment in this *h*-BN/ITO LC cell, the cell was rotated under the crossed polarized microscope to record the change in the transmitted intensity through the cell at every 2° rotation step, and the results are presented in Figs. 3(c), 3(d), 3(e), and 3(f). The angle between the average LC director, $\hat{n}$ in the *h*-BN/ITO LC cell and the analyzer is defined by θ. Figure 3(c), (d), and (e) are the micrographs of the LC texture in the h-BN/ITO cell, where $\theta = 45°$, $45° < \theta < 90°$,

and $\theta = 90°$, respectively. The graph in Fig. 3(f) shows the normalized transmitted intensity of the *h*-BN/ITO LC cell under the crossed polarized microscope as a function of θ. Clearly, Fig. 3(c) exhibits a bright uniform texture of the LC as $\hat{n}$ is at 45° with respect to the crossed polarizers. When the sample is further rotated by 45°, $\hat{n}$ becomes parallel to the polarizer, which clearly reveals a dark uniform texture in Fig. 3(e). This is the same optical behavior of the LC texture in a standard rubbed PI/ITO cell under the crossed polarized optical microscope [23]. This transition of the transmitted intensity from a uniform bight texture to a uniform dark texture at every 45° rotation confirms that 2D *h*-BN imposes a uniform planar-alignment on the nematic phase due to the hexagonal symmetry matching between the LC's benzene rings and the *h*-BN's honeycomb structure.
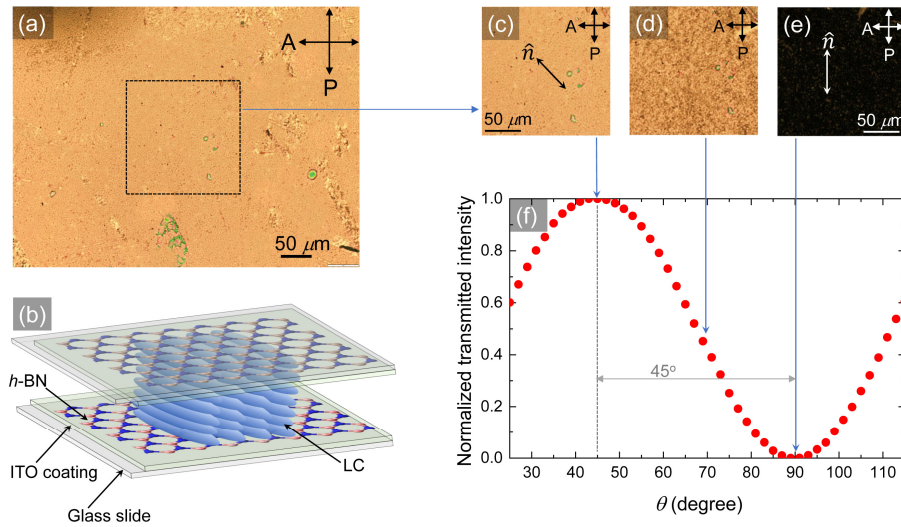

Fig. 3. (a) Crossed polarized micrograph of LC E7 in the *h*-BN/ITO cell which showed the best uniform planar-alignment. The dotted square area is used for further analysis. (b) A schematic representation of the *h*-BN/ITO cell containing a layer of ITO and an *h*-BN film on each glass slide. (c), (d), and (e) Micrographs of the bright, intermediate, and dark states, respectively, as the *h*-BN/ITO LC cell was rotated under the crossed polarized optical microscope. (h) Normalized transmitted intensity as a function of θ, the angle between the average LC director, $\hat{n}$ in the cell and the analyzer.

2.2 Electro-optical effect of LC in h-BN/ITO cell

We now show that the *h*-BN/ITO LC cell exhibits the typical electro-optical effect—which is essential for the LCD technology. The electrically-controlled birefringence effect (ECBE) [33] in an LC is observed when $\hat{n}$ rotates from the initial planar orientation to homeotropic orientation as the applied electric field in the cell exceeds its threshold value. As $\hat{n}$ rotates, the LC's effective birefringence, $\langle\Delta n\rangle$ changes as a function of applied voltage. If $\hat{n}$ is initially oriented at 45° with the crossed polarizers, then the transmitted intensity at the exit of the analyzer varies as [33]

$$I = I_O \sin^2\left(\frac{\pi d \langle\Delta n\rangle}{\lambda}\right) \qquad (1)$$

where I_o is the intensity of the plane polarized light incident on the LC cell, d is the cell-gap, and λ is the wavelength of the monochromatic light. As $<\Delta n>$ changes during the rotation of $\hat{n}$ in the presence of the applied field, a change in the phase difference, $\Delta\phi = \dfrac{2\pi d \Delta n}{\lambda}$ causes an oscillatory optical signal at the exit of the analyzer. The ECBE of LC E7 in the h-BN/ITO cell was studied using an optical setup consisted of a 5-mW He-Ne laser beam ($\lambda = 633$ nm) that passed through a polarizer, the h-BN/ITO LC cell (where is $\hat{n}$ oriented at 45° with respect to the polarizer), a crossed analyzer, and into a photodetector which was connected to a dc voltmeter to measure the transmitted intensity, I. The applied ac voltage ($f = 1000$ Hz) across the cell was ramped up, and the change in I was detected from the dc voltmeter. This experiment was also carried out under the crossed polarized microscope (with a white light source instead of the laser) to take several micrographs of the h-BN/ITO cell at different applied voltages. Figure 4 represents the ECBE of LC E7 in the h-BN/ITO cell. Figures 4(a), 4(b), 4(c), 4(d), 4(e), and 4(f) show the micrographs of the LC texture in the h-BN/ITO cell under the crossed polarized microscope at different ac voltages. Figure 4(g) exhibits the transmittance, $\dfrac{I}{I_o}$ of LC E7 in the h-BN/ITO cell as a function of the applied ac voltage. The top inset in Fig. 4(g) schematically shows the ECBE experimental setup. The transmittance curve clearly follows the oscillatory response according to Eq. (1). The intensities of the micrographs do not directly correspond to the transmittance curve, as the micrographs were taken under a white light, and the transmittance curve was obtained using a red laser (*i.e.*, a monochromatic source).
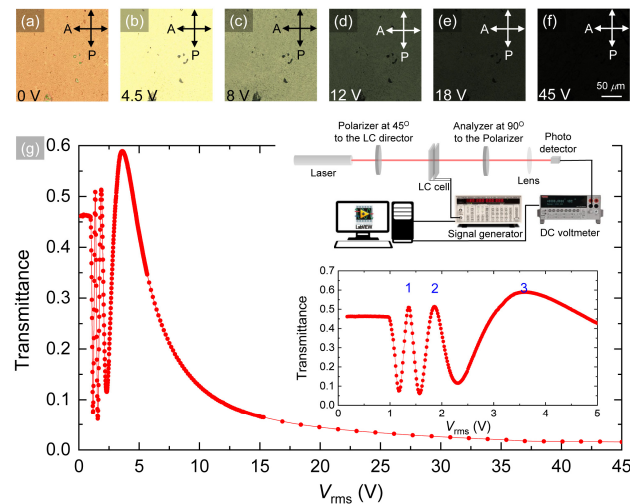

Fig. 4. Electrically-controlled birefringence effect of LC E7 in the h-BN/ITO cell. (a), (b), (c), (d), (e), (f) Micrographs of the h-BN/ITO LC cell filled with LC E7 under the crossed-polarized optical microscope at 0 V, 4.5V, 8V, 12 V, 18V, and 45 V, respectively. (g) The transmittance, $\dfrac{I}{I_o}$ of LC E7 ($T = 20°$ C) in the h-BN/ITO cell as a function of applied ac voltage ($f = 1000$ Hz). The top inset shows the experimental setup. The bottom inset shows the same transmittance curve in a smaller voltage range where three maxima can be clearly counted.

When $\hat{n}$ rotates from the planar state to the homeotropic state as the applied voltage increases, the number of maxima that appears in the transmittance curve in Fig. 4(g) is given

by $\dfrac{d\Delta n}{\lambda}$ [33]. Now, using our experimental parameters, $\Delta n = 0.225$ for LC E7, $\lambda = 633$ nm

for the He-Ne laser and, the h-BN/ITO cell-gap, $d = 9$ μm, we obtain $\dfrac{d\Delta n}{\lambda} \approx 3$. The bottom

inset in Fig. 2(g) presents the same transmittance curve in a smaller voltage range. This inset depicts *three* maxima, confirming a complete director rotation from the planar state to the homeotropic state in the cell. The inset also shows a typical Fréedericksz transition upon the application of an electric field across the cell. The results indicate that the h-BN/ITO cell exhibits the required ECBE for an LC device—where the 2D h-BN films at both sides act as the planner-alignment agent.

2.3 Measuring typical LC parameter in the electro-optic h-BN/ITO cell

Next, we show that the typical LC parameters, such as the dielectric anisotropy, splay elastic constant, and bend elastic constant, can be successfully obtained using this h-BN/ITO cell. A commercially available LC cell ($d = 9$ μm, *Instec, Inc*.) with the conventional planar PI alignment agent was used to make a proper comparison with the h-BN/ITO cell. This commercial PI/ITO cell was also filled with LC E7.

The nematic phase shows dielectric anisotropy [34], $\Delta\varepsilon = \varepsilon_{\parallel} - \varepsilon_{\perp}$, where $\varepsilon_{\parallel}$ and $\varepsilon_{\perp}$ are the dielectric components parallel and perpendicular to $\hat{\boldsymbol{n}}$, respectively. LC E7 is a positive anisotropic material with $\Delta\varepsilon = +13.8$ [35] at $T = 20°$C. An ac capacitance bridge technique [36] was employed to measure the dielectric constant, ε of LC E7 as a function of the applied ac voltage at 1000 Hz in the nematic phase ($T = 20°$C), in both the cells. The ac voltage (and not dc) was applied to prevent the effect of ion migration from influencing the dielectric measurements. The dielectric constant of the LC in both the cells as a function of the applied voltage is presented in Fig. 5(a). The dielectric data exhibit the Fréedericksz transition above the threshold voltage, $V_{\text{th}} = 0.941$ V for the h-BN/ITO cell, and $V_{\text{th}} = 0.824$ V for the PI/ITO cell, as shown in the top inset in Fig. 5(a). This confirms the fact that the 2D h-BN, as the planar-alignment agent, adequately supplies the polar anchoring energy, which can be overcome by V_{th}. The sharp Fréedericksz transition clearly shows that the pretilt angle in the h-BN/ITO cell is negligible. For a constant cell-gap, the polar anchoring strength coefficient, $W_{\theta} \propto V_{\text{th}}^2$ [25,37]. Note that $V_{\text{th (}h\text{-BN/ITO)}} > V_{\text{th (PI/ITO)}}$, which indicates that W_{θ} between the LC and the 2D h-BN is higher than that between the LC and the rubbed PI.

The average value of ε below V_{th} is $\varepsilon_{\perp}$, as shown by the arrow in Fig. 5(a). The value of $\varepsilon_{\parallel}$ can be determined from the *extrapolated* intercept of the ε vs. V^{-1} curve, as shown in Fig. 5(b). The solid line represents the linear fit in the linear regime of the ε vs. V^{-1} curve. The extrapolated y-intercept of the linear fit gives the value of $\varepsilon_{\parallel}$, as shown in Fig. 5(b). The LC orientations in the h-BN/ITO cell for $\varepsilon_{\perp}$ and $\varepsilon_{\parallel}$ are schematically illustrated in Figs. 5(a) and 5(b), respectively. Using the values of $\varepsilon_{\perp}$ and $\varepsilon_{\parallel}$, we calculate $\Delta\varepsilon = +13.3$ ($T = 20°$C) for the h-BN/ITO cell and $\Delta\varepsilon = +13.4$ ($T = 20°$C) for the PI/ITO cell. These values are within 3% of the reported value of $\Delta\varepsilon$ for LC E7 [35].

The polar anchoring strength coefficient, W_{θ} was obtained for LC E7 using the dielectric components, $\varepsilon_{\perp}$ and $\varepsilon_{\parallel}$, and threshold voltage, V_{th} employing the capacitance method described elsewhere [25,37]. It is found that $W_{\theta} = 3.5 \times 10^{-5}$ J/m^2 for the PI/ITO cell, and $W_{\theta} = 5.0 \times 10^{-5}$ J/m^2 for h-BN/ITO cell.

The Fréedericksz transition method was employed to extract the splay (K_{11}) and bend (K_{33}) elastic constants using this dielectric (capacitive) data for both the cells by fitting the capacitance (C) vs. voltage (V) graph according to the equation [38,39]

$$\frac{C}{C_O} = \frac{2}{\pi}\sqrt{1+\gamma\sin^2\varphi_m}\,\frac{V_{th}}{V}\int_{\varphi_o}^{\varphi_m}\sqrt{\frac{(1+\gamma\sin^2\varphi)(1+\kappa\sin^2\varphi)}{\sin^2\varphi_m-\sin^2\varphi}}\,d\varphi \qquad (2)$$

where C_o is the zero-field capacitance, φ_o is the pre-tilt angle, φ is the angle between $\hat{\boldsymbol{n}}$ and the substrate at V, φ_m is the maximum angle in the middle of the cell, $\gamma = \Delta\varepsilon/\varepsilon_\perp$, $\kappa = (K_{33}/K_{11}) - 1$. From this fitting, we obtain $K_{11} = 10.4$ pN and $K_{33} = 20.3$ pN for the h-BN/ITO cell. Similarly, for the PI/ITO cell, $K_{11} = 10.1$ pN and $K_{33} = 19.8$ pN. These values are within 5% of the reported values of K_{11} and K_{33} for LC E7 [35] at $T = 20°$C. Therefore, the extracted values of $\Delta\varepsilon$, K_{11}, and K_{33} of LC E7 suggest that the h-BN/ITO cell can be used reliably to characterize a nematic LC.
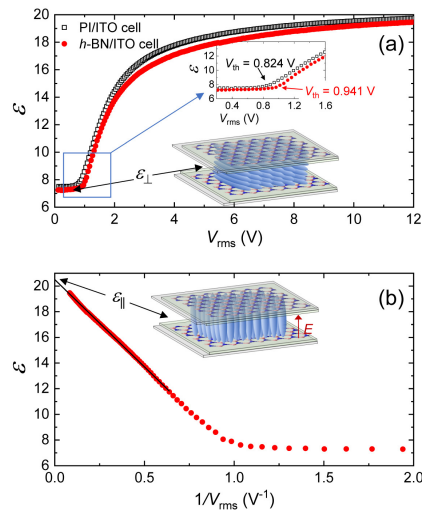

Fig. 5. (a) Dielectric constant, ε as a function of V_{rms} ($f = 1000$ Hz) in the nematic phase ($T = 20°$ C) of LC E7 in both the cells listed in the legend. The top inset shows the Fréedericksz threshold voltage, V_{th} for both the cells. The bottom inset shows the schematic representation of the planar orientation of the LC in the h-BN/ITO cell when the applied voltage is below V_{th}. (b) Dielectric constant, ε as a function of $1/V_{rms}$ for the h-BN/ITO cell. The solid line represents the linear fit in the high-voltage linear regime (as $1/V_{rms} \to 0$, $V_{rms} \to \infty$). The extrapolated y-intercept of the linear fit gives the value of $\varepsilon_\parallel$. The inset shows the schematic representation of the homeotropic orientation of the LC in the h-BN/ITO cell for a very high applied voltage.

2.4 Optical transmission spectroscopy of the electro-optic h-BN/ITO cell

Finally, we show that the h-BN/ITO LC cell exhibits more optical transparency than the commercial PI/ITO LC cell. The optical transmission spectra of the LC-filled commercial PI/ITO cell and the LC-filled h-BN/ITO cell were taken separately using FLAME-S-XR1-ES (*Ocean Optics, Inc.*) spectrometer and DH-2000-BAL UV-VIS-NIR (*Ocean Optics, Inc.*) light source. The transmission spectra for these cells in the wavelength (λ) range from 300 nm (UV) to 1000 nm (near IR) are shown in Fig. 6. The h-BN/ITO cell clearly indicates more optical transparency than the commercial PI/ITO cell, as shown in Fig. 6. In the commercial cell, the total thickness of the two rubbed planar-aligning PI (KPI-300B, *Kelead Photoelectric Materials Co., Ltd.*) layers was about 120 nm. On the other hand, the thickness of a 2D h-BN film is around 0.3 nm [40]. Replacing both the PI alignment layers with the 2D h-BN on both sides decreases this effective thickness to less than 1 nm—which leads to the potential to reduce the transmissive losses over a broad spectral range in the electro-optic LC device.
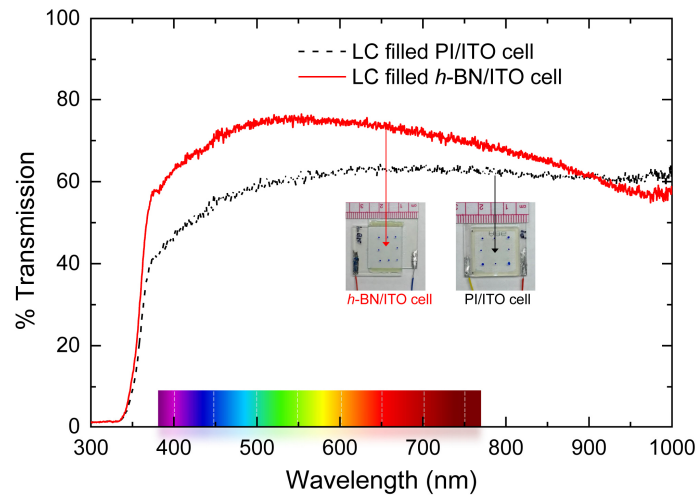
Fig. 6. Optical transmission as a function wavelength for the LC-filled PI/ITO cell and the LC-filled *h*-BN/ITO listed in the legend. The visible wavelength range is shown in the *x*-axis. The inset pictures show the two cells.

3. Conclusion

It is shown that the 2D *h*-BN can function as the planar-alignment agent in an LC cell. The appearance of the uniform planar-alignment in the *h*-BN/ITO cell and its absence in the ITO/ITO cell is a clear indication that 2D *h*-BN can serve as the planar-alignment agent. This *h*-BN/ITO cell shows a typical Fréedericksz transition with the standard electro-optical effect when an electric field is applied across the cell. The higher threshold voltage in the *h*-BN/ITO cell indicates that the planar anchoring energy between LC—*h*-BN is stronger than that in LC—PI. The measured LC parameters in the *h*-BN/ITO cell are found to be within the acceptable range for LC E7. The optical transmission spectroscopy reveals that the 2D *h*-BN as the planar-alignment agent offers the potential to decrease the transmissive losses, optimizing throughput of light over a broad spectral range in the *h*-BN/ITO cell—which may have potential applications for modern transmissive electro-optic LC devices. The presented results on the *h*-BN induced planar-alignment are expected to advance the methodology toward nanoscale manipulation of LCs in electro-optic devices using their interactions with 2D hexagonal nanomaterials, such as *h*-BN.

Disclosures

The authors declare that there are no conflicts of interest related to this article.

References

1. K. Takatoh, M. Hasegawa, M. Koden, N. Itoh, R. Hasegawa, and M. Sakamoto, *Alignment Technology and Applications of Liquid Crystal Devices* (Taylor & Francis, 2005).
2. A. Schenning, G. P. Crawford, and D. J. Broer, *Liquid Crystal Sensors* (Taylor & Francis Group, 2018).
3. H.-S. Park and K.-C. Shin, "Liquid Crystal Cell Process" in *Flat Panel Display Manufacturing*, Jun Souk, Shinji Morozumi, Fang-Chen Luo, and Ion Bita, eds. (John Wiley & Sons, Ltd., 2018).
4. J.-H. Kim and C. Rosenblatt, "Temperature effect on a rubbed polyimide alignment layer," J. Appl. Phys. **87**(1), 155–158 (2000).

5. N. A. J. M. Van Aerle, "Influence of polyimide orientation layer material on the liquid crystal resistivity in LCDs," Mol. Cryst. Liq. Cryst. (Phila. Pa.) **257**(1), 193–208 (1994).
6. V. G. Chigrinov, V. M. Kozenkov, and H.-S. Kwok, *Photoalignment of Liquid Crystalline Materials: Physics and Applications* (John Wiley & Sons, Ltd., 2008).
7. L. H. Li and Y. Chen, "Atomically Thin Boron Nitride: Unique Properties and Applications," Adv. Funct. Mater. **26**(16), 2594–2608 (2016).
8. Y. Lin and J. W. Connell, "Advances in 2D boron nitride nanostructures: nanosheets, nanoribbons, nanomeshes, and hybrids with graphene," Nanoscale **4**(22), 6908–6939 (2012).
9. G. R. Bhimanapati, N. R. Glavin, and J. A. Robinson, "2D Boron Nitride: Synthesis and Applications," Semicond. Semimet. **95**, 101–147 (2016).
10. A. Pakdel, C. Zhi, Y. Bando, and D. Golberg, "Low-dimensional boron nitride nanomaterials," Mater. Today **15**(6), 256–265 (2012).
11. X. Wang, C. Zhi, Q. Weng, Y. Bando, and D. Golberg, "Boron Nitride Nanosheets: novel Syntheses and Applications in polymeric Composites," J. Phys. Conf. Ser. **471**, 012003 (2013).
12. C. R. Dean, A. F. Young, I. Meric, C. Lee, L. Wang, S. Sorgenfrei, K. Watanabe, T. Taniguchi, P. Kim, K. L. Shepard, and J. Hone, "Boron nitride substrates for high-quality graphene electronics," Nat. Nanotechnol. **5**(10), 722–726 (2010).
13. J. Xue, J. Sanchez-Yamagishi, D. Bulmash, P. Jacquod, A. Deshpande, K. Watanabe, T. Taniguchi, P. Jarillo-Herrero, and B. J. LeRoy, "Scanning tunnelling microscopy and spectroscopy of ultra-flat graphene on hexagonal boron nitride," Nat. Mater. **10**(4), 282–285 (2011).
14. R. Decker, Y. Wang, V. W. Brar, W. Regan, H.-Z. Tsai, Q. Wu, W. Gannett, A. Zettl, and M. F. Crommie, "Local electronic properties of graphene on a BN substrate via scanning tunneling microscopy," Nano Lett. **11**(6), 2291–2295 (2011).
15. Q. Van Le, J.-Y. Choi, and S. Y. Kim, "Recent advances in the application of two-dimensional materials as charge transport layers in organic and perovskite solar cells," FlatChem **2**, 54–66 (2017).
16. G. J. Choi, Q. Van Le, K. S. Choi, K. C. Kwon, H. W. Jang, J. S. Gwag, and S. Y. Kim, "Polarized Light-Emitting Diodes Based on Patterned MoS$_2$ Nanosheet Hole Transport Layer," Adv. Mater. **29**(36), 1702598 (2017).
17. Q. V. Le, T. P. Nguyen, M. Park, W. Sohn, H. W. Jang, and S. Y. Kim, "Bottom Up Synthesis of MeSx Nanodots for Optoelectronic Device Applications," Adv. Opt. Mater. **4**(11), 1796–1804 (2016).
18. M. Arslan Shehzad, D. Hoang Tien, M. Waqas Iqbal, J. Eom, J. H. Park, C. Hwang, and Y. Seo, "Nematic liquid crystal on a two dimensional hexagonal lattice and its application," Sci. Rep. **5**(1), 13331 (2015).
19. D. W. Kim, Y. H. Kim, H. S. Jeong, and H.-T. Jung, "Direct visualization of large-area graphene domains and boundaries by optical birefringency," Nat. Nanotechnol. **7**(1), 29–34 (2011).
20. J. S. Yu, D. H. Ha, and J. H. Kim, "Mapping of the atomic lattice orientation of a graphite flake using macroscopic liquid crystal texture," Nanotechnology **23**(39), 395704 (2012).
21. Y. J. Lim, B. H. Lee, Y. R. Kwon, Y. E. Choi, G. Murali, J. H. Lee, V. L. Nguyen, Y. H. Lee, and S. H. Lee, "Monitoring defects on monolayer graphene using nematic liquid crystals," Opt. Express **23**(11), 14162–14167 (2015).
22. R. Basu, D. Kinnamon, and A. Garvey, "Graphene and liquid crystal mediated interactions," Liq. Cryst. **43**(13–15), 2375–2390 (2016).
23. R. Basu and S. A. Shalov, "Graphene as transmissive electrodes and aligning layers for liquid-crystal-based electro-optic devices," Phys. Rev. E **96**(1-1), 012702 (2017).
24. R. Basu and A. Lee, "Ion trapping by the graphene electrode in a graphene-ITO hybrid liquid crystal cell," Appl. Phys. Lett. **111**(16), 161905 (2017).
25. R. Basu, "Enhancement of polar anchoring strength in a graphene-nematic suspension and its effect on nematic electro-optic switching," Phys. Rev. E **96**(1-1), 012707 (2017).
26. R. Basu, D. Kinnamon, N. Skaggs, and J. Womack, "Faster in-plane switching and reduced rotational viscosity characteristics in a graphene-nematic suspension," J. Appl. Phys. **119**(18), 185107 (2016).
27. K. A. Park, S. M. Lee, S. H. Lee, and Y. H. Lee, "Anchoring a Liquid Crystal Molecule on a Single-Walled Carbon Nanotube," J. Phys. Chem. C **111**(4), 1620–1624 (2007).
28. R. Basu and A. Garvey, "Insulator-to-conductor transition in liquid crystal-carbon nanotube nanocomposites," J. Appl. Phys. **120**(16), 164309 (2016).
29. M. A. Shehzad, S. Hussain, J. Lee, J. Jung, N. Lee, G. Kim, and Y. Seo, "Study of Grains and Boundaries of Molybdenum Diselenide and Tungsten Diselenide Using Liquid Crystal," Nano Lett. **17**(3), 1474–1481 (2017).
30. X. Li, Y. Zhu, W. Cai, M. Borysiak, B. Han, D. Chen, R. D. Piner, L. Colombo, and R. S. Ruoff, "Transfer of large-area graphene films for high-performance transparent conductive electrodes," Nano Lett. **9**(12), 4359–4363 (2009).
31. X. Liang, B. A. Sperling, I. Calizo, G. Cheng, C. A. Hacker, Q. Zhang, Y. Obeng, K. Yan, H. Peng, Q. Li, X. Zhu, H. Yuan, A. R. H. Walker, Z. Liu, L.-M. Peng, and C. A. Richter, "Toward clean and crackless transfer of graphene," ACS Nano **5**(11), 9144–9153 (2011).
32. Desktop LCD Display Comparison, http://www.prismo.ch/comparisons/desktop.php
33. L. M. Blinov and V. G. Chigrinov, *Electro-optic Effects in Liquid Crystal Materials* (Springer-Verlag, 1996).
34. P. G. De Gennes and J. Prost, *The Physics of Liquid Crystals* (Oxford University, 1995).
35. Data Sheet Licristal® E7, Merck KGaA, Germany, 2001.

36. R. Basu and G. S. Iannacchione, "High-resolution dielectric spectroscopy and electric-field dependence of carbon allotropes including multi-wall and single-wall nanotubes," Appl. Phys. Lett. **92**(5), 052906 (2008).

37. A. Murauski, V. Chigrinov, A. Muravsky, F. S.-Y. Yeung, J. Ho, and H.-S. Kwok, "Determination of liquid-crystal polar anchoring energy by electrical measurements," Phys. Rev. E Stat. Nonlin. Soft Matter Phys. **71**(6 Pt 1), 061707 (2005).

38. D. Demus, J. Goodby, G. W. Gary, H.-W. Spiess, and V. Vill, *Physical Properties of Liquid Crystals* (Wiley-VCH, 1999).

39. R. Basu, D. Kinnamon, and A. Garvey, "Nano-electromechanical rotation of graphene and giant enhancement in dielectric anisotropy in a liquid crystal," Appl. Phys. Lett. **106**(20), 201909 (2015).

40. L. Britnell, R. V. Gorbachev, R. Jalil, B. D. Belle, F. Schedin, M. I. Katsnelson, L. Eaves, S. V. Morozov, A. S. Mayorov, N. M. R. Peres, A. H. C. Neto, J. Leist, A. K. Geim, L. A. Ponomarenko, and K. S. Novoselov, "Electron tunneling through ultrathin boron nitride crystalline barriers," Nano Lett. **12**(3), 1707–1710 (2012).